ACT WIND TUNNEL EXPERIMENTS OF A TRANSPORT-TYPE WING

T.Ueda, H.Matsushita, S.Suzuki, Y.Miyazawa
National Aerospace Laboratory
Chofu,Tokyo,Japan
and
Y.Matsuzaki
Nagoya University
Nagoya,Japan

Abstract

This paper summarizes the wind tunnel experiments on the active control technology that have been conducted in the large low-speed wind tunnel in National Aerospace Laboratory. The experiments include a gust load alleviation (GLA) and two active flutter suppression (AFS) tests.

A cantilevered elastic wing model is desinged to simulate an energy efficient transport. The model has two control surfaces which are independently driven by small electric torque motors. In the GLA tests against the Dryden-type random gust, 25% reduction of bending moment in RMS values at the wing root was attained by a single aileron control. In the second AFS test, flutter boundary was raised up by 13% in speeds when two control surfaces were activated simultaneously. It was found that the leading-edge control surface was very effective for the AFS. Unique devices of a gust generator and a flutter stopper were installed in the tunnel for these ACT tests.

1. Introduction

Technologies have been undergoing progressive innovations in every fields of aviation. Among them is the active control technology, which has a prominent possibility for improving the aircraft performance and safety[1-2].

During these several years, research on the active controls of an aeroelastic system has been continuously pursued in National Aerospace Laboratory as illustrated in Fig.1. Prior to the experimental works, some theoretical studies relating to the active aeroelastic control have been performed to establish the design methodology for the aeroelastic controller. They included the unsteady aerodynamic modeling[3-5], the synthesis of active aeroelastic controls and the aeroelastic system identifications[6]. An experimental research program concentrating on the gust load alleviation and the active flutter suppression began in 1982, being based on those theretical investigations. Main objective of the program is to validate and to improve the analytical tools that have been compiled in the preceding theoretical studies.

For the first two years, conducted was a preliminary study on the gust load alleviation with a rectangular wing by utilizing the Gust Wind Tunnel. The analysis was able to predict the experimental results with sufficient accuracy for that model. The bending moment at the wing root was alleviated by approximatly 45% in the RMS value[7]. Since 1984, a series of wind tunnel experiments of a transport-type wing has been conducted to develop more realistic techniques on the active controls. The present report summarizes the essence of the three experiments.

2. Wind tunnel Model of a Cantilevered Wing

A planform of the elastic model used in the experiments is depicted in Fig.2. It simulates a future type of energy efficient transports with an high aspect ratio of 10.5 and a rather modest swept angle of 18 degrees at the quater-chord line[8]. The scale factor is about 1/9. Stiffeness distributions are provided at 40% chord line by an aluminum alloy spar which is formed with four thin plates and a flange by adhisive bonding. Seventeen balsa wood seguments are shaping NACA0012 airfoil covering the spar. Two housings of the control surface actuator are embedded in the spar as shown in Fig.3. The wing has two partial span control surfaces, one at the leading-edge of 15% chord between the spanwise ninth and eleventh segments and one at the trailing edge of 73% chord. The model furnishes two options for the trailing-edge surface (ailerons) ,i.e. one at the same spanwise location as the leading-edge control surface and the other from the eleventh to thirteenth wing segments a little outer than the previous one. During the GLA test of early stage, only one actuator was mounted in the motor housing with a dummy weight in the other. The second actuator was added later in AFS tests. Therefore, five combinations among the locations of ailerons and actuators have occurred during the tests. These configurations are listed in Table 1.

Two accelerometers of piezoresistive type which have been equipped on the wing spar at a spanwise station 1132 are used as a feed back sensor. Strain signals of wing responses are also used to obtain the additional drive-input for the aileron actuator in the GLA tests. Locations for these sensors have been shown in Fig 2.

3. Mathematical Model

3-1 Structural Dynamics

A mathematical model of the elastic wing structure was first formulated by the FEM on the primitive design data.

$$M \ddot{d} + K d = 0 \tag{1}$$

In the stiffness matrix K of the equation above, the gravity effect was accounted for by means of the geometric stiffness matrix since the model is set upright on the tunnel floor. The gravity force decreases the natural frequencies with fundamental bending modes by 5% at most. Although it does not affect much the structural characteristics, it causes an unexpected effect on control laws as will be described later.

In order to find more accurate math model, structural tests were carried out on stiffness distributions and on vibrations. Then, the mass and stiffness matrices in Eq.(1) were tuned in accordance with these test results. Typical

results of the vibration test and FEM calculations are illustrated Fig.4. By using the mass and stiffness matrices thus obtained, four eigenmodes with lower frequencies are computed to provide the generalize coordinates for the wing model structure.

$$d = \sum_{i=1}^{4} q_i \, d_i \qquad (2)$$

Four may be the minimum number of modes that can analyze the flutter of this wing since the first torsional vibration appears as the fourth mode. By adding model damping coefficients that have been obtained in the vibration test, the structural dynamics of the wing model can be written as

$$\frac{1}{\omega_i^2} \ddot{q}_i + \frac{2\zeta_i}{\omega_i} \dot{q}_i + q_i + s_{1i} \ddot{\delta}_1 + s_{2i} \ddot{\delta}_2 = f_i$$

$$(i=1,..,4) \qquad (3)$$

where ω_i and ζ_i are the natural frequency and modal damping of the ith mode, respectively, and δ_1 and δ_2 denote the deflection angles of the leading-edge and trailing-edge control surfaces, respectively. The dynamical coupling terms s_{ni} and the generalized force f_i will be discussed below.

3-2 Dynamic Structural Coupling of Control Surfaces

Although the dynamic coupling between the wing structure and the control surface movement can be considered much less in real wings, the dynamic unbalance of contol surfaces including the reaction of the torque motors causes appreciable structural coupling in this very flexible model. Therefore, it is relevant to obtain an accurate math model with high fidelity to the model structure even if the characteristics are peculiar to the wind tunnel model itself. The amount of coupling, s_{ni}, in Eq.(3) can be determined from the acceleration response due to the aileron excitation. A frequency response of accelerometers a_m due to the aileron movements can be assumed as

$$\frac{\hat{a}_m}{\delta_n} = -\sum_{i=1}^{4} \frac{z_{mi} \omega^4 \omega_i^2 s_{ni}}{\omega_i^2 - \omega^2 + 2j\zeta_i\omega_i\omega} \qquad (n,m=1,2) \qquad (4)$$

where j is the imaginary unit and z_{mi} indicates a component of displacement at the accelerometer a_m location, associated with the i-th generalized coordinate. The coefficients in Eq.(4) can be adjusted so that the response curve given by Eq.(4) should best fit with the measured transfer function. · An example result of this procedure is shown in Fig.5. The transfer function was measured during the time when the actuator was randomly excited and analysed between the two signals with the accelerometer and a rotary potentiometer of the control surface. In the curve fitting process, however, we cannot separate the coefficient s_{ni} from $z_{mi} s_{ni}$ at once. One way of separating this is to use the theoretical value for z_{mi} that can be calculated by using the eigenmodes. Then the dynamical coupling can be obtained with respect to every i-th mode. In order to examine the accuracy of the quantity thus obtained, the response curve calculated with these values has been compared with the measurements of another accelerometer a_2 as shown in Fig.6, which demonstrates a certain validity of

the procedure.

3-3 Actuator Dynamics

As the actuators to drive control surfaces, two small D.C. tonque motors with the magnet made of samarium-cobalt are utilized together with the position-feed-back servomechanism. Their power axes are linked to the drive shafts of control surfaces through the reduction gears. These actuation units have been carefully assembled to avoid free play which causes unpreferable effects on the control system. Figure 7 illlustrates the measured frequency responses of the actuation units. As can be seen, the dynamics slightly depends on the amplitude. However, they show fairly flat characteristics up to well above the flutter frequencies which will be around 6~8 Hz for this model. The actuator may be modeled by a typical second order differential equation,

$$\frac{1}{\omega_\delta^2} \ddot{\delta}_n + \frac{2\zeta_\delta}{\omega_\delta} \dot{\delta}_n + \delta_n = \delta_{cn} \qquad (n=1,2) \qquad (5)$$

where ω_δ and ζ_δ assumes $2\pi \times 25$ rad/s and 0.7, respectively.
This math model is also depictd in Fig.7 with the solid curves.

3-4 Unsteady Aerodynamic Forces

The external generalized forces f_i in Eq.(3) consist of the unsteady aerodynamic forces due to both the wing deformation and the control surface deflection and also due to the gust. These forces must be mathematically modeled to be included in the system equation. Various methods have been studied for the modeling. We adopt here so-called Roger's approximation[9] which includes the conversion from the aerodynamic forces in the frequency domain to those in the Laplace domain. The frequency domain aerodynamic forces can be computed by the doublet-point method.[10]

If we defined the generalized force vector of nondimensionalized aerodynamic force as $\hat{c}_f$ and the generalized coordinate vector with the control surface deflections as $\hat{q}$ then Roger's approximation with one lag term gives

$$A_{model}(k) = (jk)^2 A_2 + (jk) A_1 + A_0 + \frac{1}{jk+\lambda} G,$$

$$\hat{c}_f = A_{model} \hat{q} \; ; \; \hat{c}_f \in c^4, \; \hat{q} \in c^6 \qquad (6)$$

where k is the reduced frequency defined by $b\omega/U$, and $^$ means that the quantity is in the frequecy domain. The coefficient matrices A_2, A_1, A_0 and G can be calculated from the aerodynamic matrix A that can be computed as a function of the reduced frequency. Figure 8 depicts a mesh used to obtain the aerodynamic matrix by the doublet point method. We assumed the characteristic root λ of Eq.(6) as 0.25 a priori and applied the curve fitting technique to eleven aerodynamic data with the reduced frequency from 0 to 1.
A result of the modeling is shown in Fig.9 comparing with the computational results by the

195

DPM. In the figure, the fifth and sixth indices correspond to the degree of freedom of the leading-edge control surface and the outer aileron deflections, respectively. Thus, the unsteady aerodynamic forces can be written in the time domain via an auxiliary state vector z as

$$c_f = (\frac{b}{U})^2 A_2 \ddot{q} + (\frac{b}{U}) A_1 \dot{q} + A_0 q + z$$

$$(\frac{b}{U})\dot{z} = Fz + G \tag{7}$$

where $F = \text{diag}\{-\lambda, \ldots, -\lambda\}$.

These aerodynamic math models can be verified, though in an indirect way, by comparing the frequency response due to control surface deflections in a finite flow speed. Figure 10 shows a transfer function of a_1 versus δ_1, measured in the flow speed of 30 m/s. Noisy curves and circles in the figure represent the measurements by the random and stepped-sine excitations, respectively, whereas the solid curves were obtained by the calculations with the math model. It can be said that all the differences from Fig.5 come from the aerodynamic forces. A good agreement between the measurements and the math model confirms the validity of the aerodynamic modeling.

3-5 Aerodynamics for the Gust

Aerodynamic loadings due to gusts are calculated on the assumption of a quasi-steady gust with spanwise uniform distributuions. The power spectrum of the gust is given by

$$\Phi_g(\omega) = \frac{\sigma_g^2}{\omega_g} \frac{2}{1+(\frac{\omega}{\omega_g})^2} \tag{8}$$

which can be derived by simplifying the Dryden model. A random gust with the power spectrum of Eq.(8) can be simulated by the following first order system.

$$\dot{w}_g = -\omega_g w_g + w_r \tag{9}$$

where w_r is generates a white noise of the intensity $2\omega_g \sigma_g^2$.

3-6 Measurement Noise

In a real circumstance, measurements contain error, more or less. In order to apply the LQG method for designing control laws, it is modeled as the measurement noise having the shape of white noise with a power spectrum,

$$\Phi_v(\omega) = \frac{\pi}{\omega_v} \sigma_v^2 \tag{10}$$

where the band width ω_v and the mean square are appropriately given parameters.

3-7 Total System Math Model

The math models for the structure, aerodynamics, gust and noise which were introduced in the preceding discussion yield the following total system equations with the state vector

$x^T = \{ q^T \dot{q}^T z^T w_g \}$, the measurements y and the control u.

$$\begin{cases} \dot{x} = Ax + Bu + W \\ y = Cx + Du + V \end{cases} \tag{11}$$

where W and V assume white noise vectors. Equation (11) has an appropriate form for the application of the modern control theory.

4. Test Equipment

In the early stage of ACT test program, the gust wind tunnel with a 2x2m cross-section with the cascade vanes for generating gusts has been utilized for preliminary study of the gust load alleviation. A smaller model has been used for those tests. However, for the present size of the highly mechanical model, it turned out to be too small to test without wall effects. Therefore, we decided to use a larger tunnel by newly constructing a gust generator. Figure 11 shows the schematic of the double-vane-gust-generator which are driven by a hydrauric servo acuator. Two vanes are mechanically linked to move in the same phase and can generate gusts with the frequency components up to 9.5 Hz. Vortices ejected from the vane tips create vertical gusts on the cantilevered wing which is set up on the tunnel floor.

For flutter tests, a unique device to prevent the model from destroying at flutter occurrences has been innovated in the large low speed wind tunnel. It is essential for the AFS tests to repeatedly use the same model since the control effectiveness should be examined with the rest of the parameters kept in the same condition. As depicted in Fig.12, a fence made of mesh and frame can open from the tunnel floor to defend against the main flow. It is operated with the swift response air-cylinder to respond to flutter onset. This flutter stopper worked well in the experiments. Adding to that device, we also use the snubber cord to give constraint on the model as a back-up system as illustrated in the figure. Owing to those devices,the model could experience totally fifty times of fluttering in various conditions.

5. Design of Control Laws

For the design of control laws in the active aeroelastic control systems, various approaches have been proposed.[11-15] In the present study, we designed the laws for both GLA and AFS controls by utilizing the technique of the so-called LQG method which is quite relevant to be applied to the stochastic problem of random gust response. The method also provides a unified tool for the AFS control design with the assumption of realistic measurement noise. Starting from the system equation, like Eq.(11), the method comprises an estimation of state vectors by the Kalman filter and the estimated state feedback with the optimal regurator gain. In the modern control theory of optimal controls, it sometimes raises a question how to choose the cost function, i.e. how to determine the matrix Q in the following equation.

$$J = E[\rho \frac{1}{2} x^T Q x + u^T R u] \tag{12}$$

where $R=\text{diag}\{R_1,R_2\}$.

In the present study, we render a clear physical meaning of the "energy and control power" to this cost function. Then the matrix Q becomes such that the non-zero entries are

$$Q_{ii}=1, \quad Q_{i+6,i+6} = \frac{1}{\omega_i^2} \qquad (i=1,..,4) \qquad (13)$$

The method provides the optimal control law, or the optimal controller, the order of which is equal to that of the total aeroelastic system. For practical implementation, however, this high order controller is unrealistic. Some components of the controller have little contribution to the cost function so that they can be considered dispensable.[16] The reduced order controller needs to be derived by using the cost function (12) with the same parameters which are determined through LQG control synthesis. The computational algorithm adopted here consists of two processes. One is the order reduction of the controller by an approximation by using the chained aggregation model method.[17] The other is the mathematical programming for optimization of the coefficients of the controller transfer function. For the verification of the controller finally implemented, we can resort to the conventional methods of control system analysis, such as Bode diagram, Nyquist plot, characteristic roots, and so on.

6. GLA Tests

GLA tests were conducted with a fixed flow speed of 20 m/s. With that speed, the controllability of the system was first examined analytically by the full-state feed back control. The parameter in Eq.(12) indicates a trade-off between the control power and the response alleviation against the same random gust. Figure 13 illustrates the variations of total energy in the wing response by changing the trade-off parameter. The abscissa is a root mean square of the feed back command which can be interepreted as a control amount. As can be expected, the more we use control power the lesser the wing response becomes. We can determine an adequate control gain from this chart. The figure also represents the effectiveness depending on the three configurations. The difference between two trailing-edge ailerons, configuration 1 and configuration 2, is small and they are much effective in comparisons with the leading-edge control surface, configuration 3. Considering those results, only the ailerons were used in the GLA tests. Although the results are not presented here, it can be said that more than ninety percent of the energy is associated with the first bending mode.

After the order reduction of the laws has been made, wind tunnel tests were conducted with the acceleration feed back controls called Law 1. The block diagram of the law is given in Fig.14. The test results in Fig.15. Which shows the gain and phase of a transfer function between the acceleration a_1 and the gust generator angle . The circles in the figure represent the results measured by the stopped-sine excitation while the solid and chained curves are those computed by using the math model. Since the denominator of the transfer function is the deflection angle of a

gust generator, the phase angle contains a flow conveyance delay which depends linearly on the gust frequencies. The first peak of the gain with the GLA system off corresponds to the first bending mode in the frequency of about 2 Hz. It can be seen from the figure that this peak is well attenuated when the control is active. Strangely enough, however, the control effects turn out to be opposit in the very law frequency range including the static case (zero frequency) in spite of the fact that the feed back signal is given by the accelerometers.

It may be explained that this adverse augmentation in the wing response can be attributed to the gravity field which yields a sine compoment of the gravity acceleration if a vertical wing has an inclination at the sensor position. The math model can also follow this phenomenon if the sine conponent of gravity is included in the measurement vector as shown in the figure with the solid curve. The effect cannot be eliminated by the acceleration feed back since the accelerometers cannot distinguish the gravity acceleration from the kinetic one. In order to counteract this effect, the bending strain was utilized to extract deformation from the gravity components since the strain gage can provide useful singnal in the low frequency range. The strain gage output was filterd and superimposed on the feed back signal as shown in Fig.16. The results are presented in Fig.17 in which the adverse gravity effect is completely extinguished. In this Law 2, the feed back gain for the accelerometers has been doubled to emphasize the control effects. A direct comparison in the power spectrum density of the bending moment at the gage location is made in Fig.18. The control performance resulted in a 25% reduction in the bending moment RMS.

7. AFS Tests

Two wind tunnel tests for the active flutter suppression were conducted during two years. In the first test, each control surface was activated independently to find the individual performance. In the second test conducted in the next year, the two-degrees-freedom control was tested by activating the leading-edge surface and the trailing-edge aileron simultaneonsly. A digital controller was also tried in the second test. In these flutter tests, the flutter speeds were confirmed by the following procedure. First, the flow of the wind tunnel is set at a certain speed increased by a certain amount of increment, and then, four rectangular pulse singnals in every twenty seconds were inputted to the control surface driver to make constant disturbances that may trigger flutter. Most of the onset were initiated by the pulse disturbance but some were observed while the flow speed was increasing.

The flutter speed predicted by the math model is about 36 m/s slightly depending on the configurations, whereas the wing experienced flutter at the speed around 35 m/s which also depens on the configurations. The differece may be attributed to the four mode analysis of the structure which provides a little stiffer stiffness. Design speed for obtaining the optimal controller is selected as 40 m/s. Figure 19 illustrates the root locus plots by varing the trade-off parameter in the control cost and the root loci without controls by varying the flow speed.

The root locus for the controlled system contains three sets of curves corresponding three kinds of controls, i.e. the leading-edge control surface only, the trailing-edge aileron only and the two-degrees-of-freedom control. As the weight of controls increases, every curve converges to the certain points that represent the minimum input energy control. These roots have the same positions as those without controls except the unstable torsional mode which is located at the symmetric point with respect to the imaginary axis. It can be said that, generally, if the R becomes smaller, which means if we use more control power, then the system gains more damping. The relationship between the energy in the cost (12) and the combination of two control surfaces is illustrated in Fig.20. The figure (b) shows the iso-energy level versus the coordinates of the root-mean-square deflections of two control surfaces. Since the curves with a constant sum of two mean squares depict concentric circles around the origin of coordinates, it can be seen from the figure that two-dgrees-of freedom control can more efficiently reduce the energy of the cost function than the single surface controls. Further, if we compare the leading-edge control surface and the trailing-edge aileron, the former is more effective. These characteristics were demonstrated by the wind tunnel test results. The representative results are given in Table 2. The most effective control was the two-degrees-of-freedom control which attained 13% up in flutter speeds as shown in the Table. The single leading-edge control could torrelate flutter 10% above the flutter speed of the uncontrolled wing. The predicted values computed by the math model are also given with parentheses in the Table. It can be seen that the experimental achievements were approximately one half with the flutter speed augmentation. This discrepancy may be ascribed to the aerodynamic forces due to the control surface in which we use no correction factors for the math model. If some aerodynamic correction were made such as for a control surface gap and for boundary layer effects, better agreement might be expected.

Most of the control laws were loaded in a handy analog computer. At the end of the test, a digital controller was tried also. The controller was designed specially for the present flutter control. Generally, in comparison with analog computers, digital controllers have many advantageous points such that they are tough against noise, free from drifting, easy loading of the laws, broad in the usage, compact with hardware and so on.

They possesses, however, two inherent drawbacks. One is finite processing time of computaion, and the other is discrete quantity of digitization, which may deteriorate the accuracy. For flutter controls, the former will cause appreciable delay in commands. Therefore, the digital controller for flutter was aimed at realizing super high-speed processing. It resulted in five microsecond throughput time with twelve bits AD/DA conversion. It is capable of loading maximum eighth order laws in two channels, through the GP-IB buslines. The controller was implemented in lieu of the analog computer with the same control law as EW 201. The result recorded, however, only 5% up in flutter speeds, whereas by the analog computer it was 13% as shown in Table 2. Unfortunately, due to the test schedule, we did not have sufficient time to follow up the reason of the

difference. It may come from ailiasing, phase lag, phase compensator, finite accuracy, smoothing filter, etc.

At the end of these results, a time history which demonstrates the active flutter suppression is shown in Fig.21. The figure shows the record of control by ET 303 which use the trailing-edge aileron only in the configuration 5. The flow speed was 36.5 m/s just above the flutter boundary of the uncontrolled wing. Although the feed back command for the trailing-edge aileron, which is given at the bottom in the record, was always computed during the run, the controller has been first turned off to hold the aileron at the undeflected position . No sooner the disturbance had been inputted in the leading-edge-control surface by the pulse than the wing started fluttering. Then, controller was turned on 0.53 second after the pluse disturbance, and the aileron began to suppress the flutter as clearly shown in the figure.

8. Conclusion

Three aeroelastic control tests have been described. In the gust load alleviation tests, a 25% reduction of the RMS bending moment was achieved against a realistic random gust. In the flutter control, two-degrees-of-freedom control using the leading-edge control surface and the trailing-edge aileron raised up the typical bending-torsion flutter speed by thirteen percent. This increment is thought to be significant amount of the angmentation if we consider the violent flutter of this clean wing.

The control laws were designed in a unified manner by the LQG method in which we defined the cost function as a physical quantity of the system energy and control power. The wind tunnel results proved its applicability to both GLA and AFS controls.

By these tests using a transport-type wing model, the implementation for both theoretical and experimental methodology is thought established to a certain degree. However, in the end of this conclusion, three problems to be solved may be extracted.

(1) Systematic order reduction of control laws needs to be developed and should be established.
(2) Correction on the aerodynamic forces of the control surface is needed.
(3) Control performance of digital controller may require further investigations.

Reference

(1) Hitch, H.P.Y., "Active Controls for Civil Aircraft, " Aeronautical Journal, Oct. 1979, pp. 389-398.
(2) Hwang, C. and Kesler, D. F., "Aircraft Active Controls --- New Era in Design, "Astronautics and Aeronautics,vol. 21, No.6,1983, pp. 70-85
(3) Miyazawa, Y., " Time Response Approach to Numerical Computation of Asymptotic Series in Unsteady Aerodynamics for a Lifting Surface in Incomprssible Flow," NAL TR-721T, 1982.

(4) Matsushita, H., "Aerodynamic Transfer Functions and Its Application to Active Flutter Control," Doctoral Dissertation, Dept. of Aeronautics, The University of Tokyo, 1982 in Japanese.

(5) Ueda,T.,"Expansion Series of Integral Functions Occurring in Unsteady Aerodynamics," Journal of Aircraft, Vol. 19, April 1982, pp.345-347.

(6) Matsuzaki, Y. and Ando, Y., " Estimation of Flutter Boundary from Random Response due to Turbulence at Subcritical Speeds," Journal of Aircraft, Vol. 18, Oct. 1981, pp.862-868.

(7) NAL ACT Study Group, "Gust Load Alleviation of a Cantilevered Rectangular Elastic Wing.--- wind Tunnel Experiment and Anaysis."NAL TR-846, 1984, in Japanese.

(8) Horikawa, H. and Saito, K. "A Wind Tunnel Study of Active Control Technology on a High Aspect Ratio Wing," AIAA paper No. 86-0956, 1986.

(9) Roger, K. L., "Airplane Math Modeling Method for Active Control Design," AGARD CP-228, April 1977, pp.4-1 4-11.

(10) Ueda, T. and Dowell, E. H., "A New Solution Method for Lifteing Surface in Subsonic Flow," AIAA Journal, Vol. 20, No. 3, 1982, pp. 348-355

(11) Nissim, E., " Recent Advance in Aerodynamic Energy Concept for Flutter Suppression and Gust Alleviation Using Active Controls, " NASA TN D-8519, 1977.

(12) Newsom, J. R., " A Method for Obtaining Practial Flutter-Suppression Control Laws Using Results of Optimal Control Theory,"NASA TP 1471, 1979

(13) Abel, I., " An Analytical Technique for Predicting the Characteristics of a Flexible Wing Equipped With an Active Flutter-Suppression System and Comparison With Wind-Tunnel Date," NASA TP 1367,1979.

(14) Schmidt, D. K. and Chen, T. K., "Frequency Domain Synthesis of a Robust Flutter Suppression Control Law," J. Guidance and Control, Vol.9., No.3, 1986, pp.346-350

(15) Liebst, B. S., Garrand, W. L., and Adams,W. M., "Design of an Active Flutter Suppression System,"Guidance, Control, and Dynamics, Vol.9, No.1, 1986, pp.64-71.

(16) Hyland, D.C., " The optimal prjoection approach to fixed-order compensation: numerical methods and illustrative results," AIAA paper 83-0303, 1983.

(17) Miyazawa, Y., "Chained aggregation model with minimum truncation error, " to be published in the International Journal of Control.

TABLE 1. CONFIGURATIONS

Configuration	1	2	3	4	5
Aileron	inner	outer	inner	inner	outer
Actuator	T.E.	T.E.	L.E.	both	both

TABLE 2. RESULTS OF FLUTTER CONTROL

LAW	CONTROL SURFACE	FLUTTER SPEED (m/s)	FREQUENCY (Hz)	EFFECT (%)
DL201	LEADING-EDGE	38.6 [35.2]	6.1 (6.3)	10 (20)
DT301	TRAILING-EDGE	36.4 [35.2]	6.1 (7.1)	3 (12)
EW201	BOTH	39.3 [34.8]	6.2 (6.1)	13 (24)

[ ] ··· UNCONTROLLED   ( )··· CALCULATED

FIGURE 1.   Research Program for Active Aeroelastic Control in NAL

199

FIGURE 2. Wing Model

Strain Gage for Bending
Strain Gage for Torsion
Accelerometer a_1
Accelerometer a_2
Leading Edge Control Surface δ_1
E.A. 40%
Seg. 1 Seg. 2 Seg. 3
Seg. 17
Unit(mm)
Inner Aileron
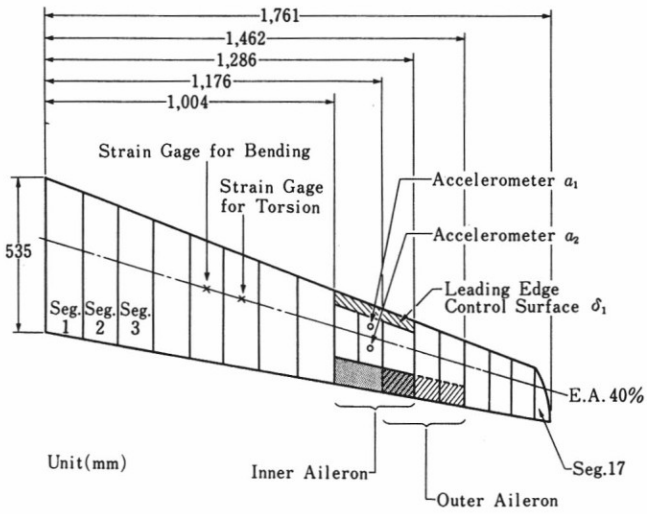Outer Aileron
535
1,761
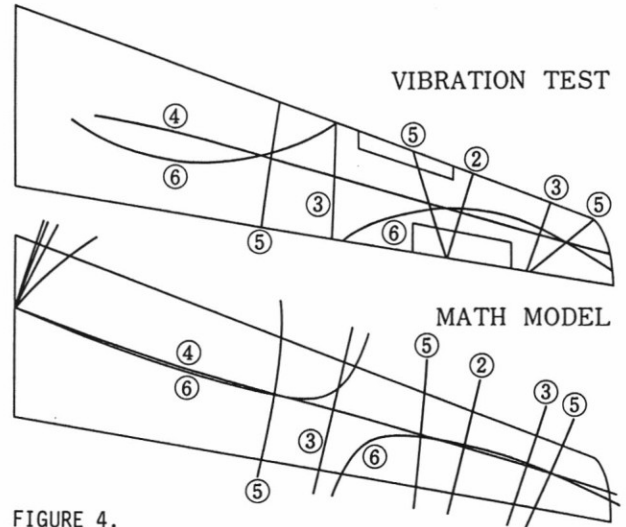1,462
1,286
1,176
1,004

VIBRATION TEST
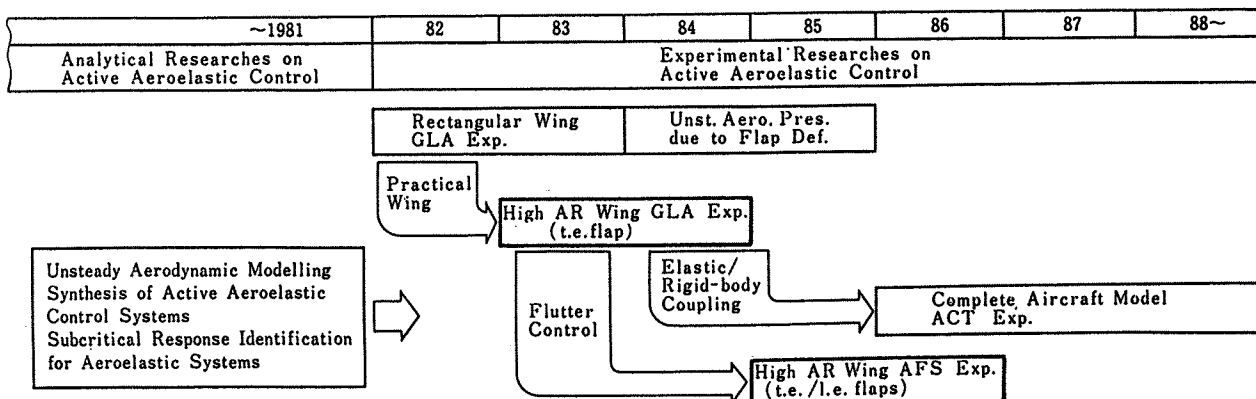
MATH MODEL

FIGURE 4.
NODAL LINES FOR CONFIGURATION 4
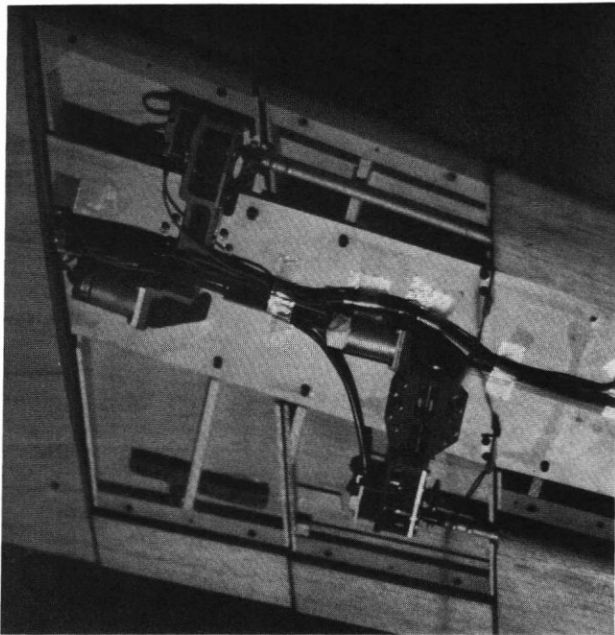
FIGURE 3. Tow Actuators on the Spar
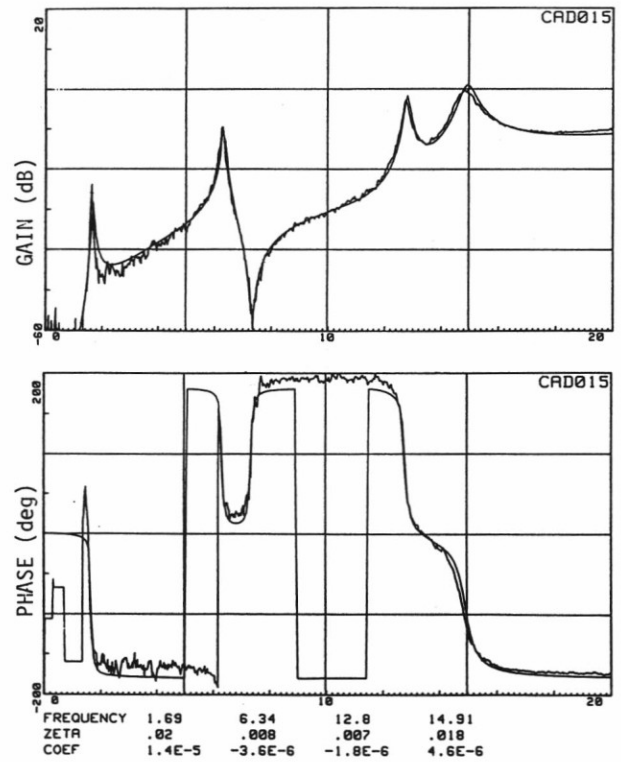
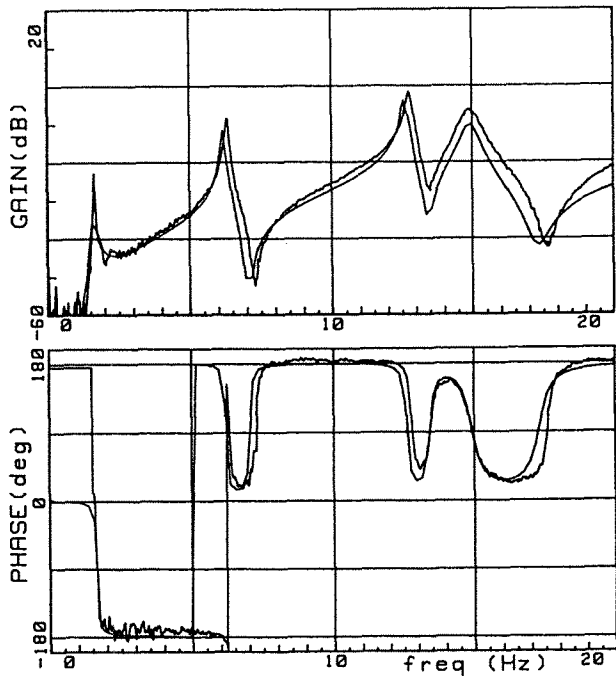FIGURE 5. Frequency Response a_1/δ_1

FREQUENCY	1.69	6.34	12.8	14.91
ZETA	.02	.008	.007	.018
COEF	1.4E-5	-3.6E-6	-1.8E-6	4.6E-6

CAD015

GAIN (dB)

PHASE (deg)

200

FIGURE 6. Frequency Response a_2/δ_1

BODE DIAGRAM

Math Model ($\omega_\ell = 25(2\pi)$ rad/s, $\zeta = 0.7$)

Exp. Amp.
--□-- 0.9°
--○-- 3.2°
--△-- 6.2°
--◇-- 12.6°

GAIN (dB)

PHASE (deg)

HERTZ
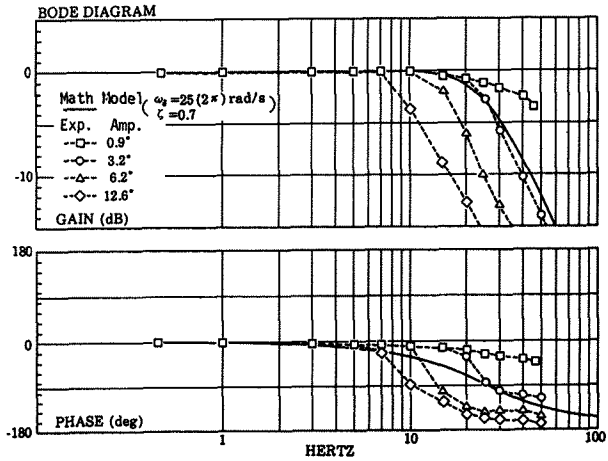
FIGURE 7. Actuator Frequency Response

192 ELEMENTS
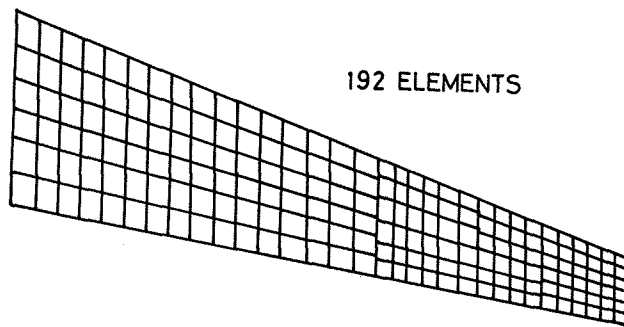
FIGURE 8. Doublet-Point Method Calculation
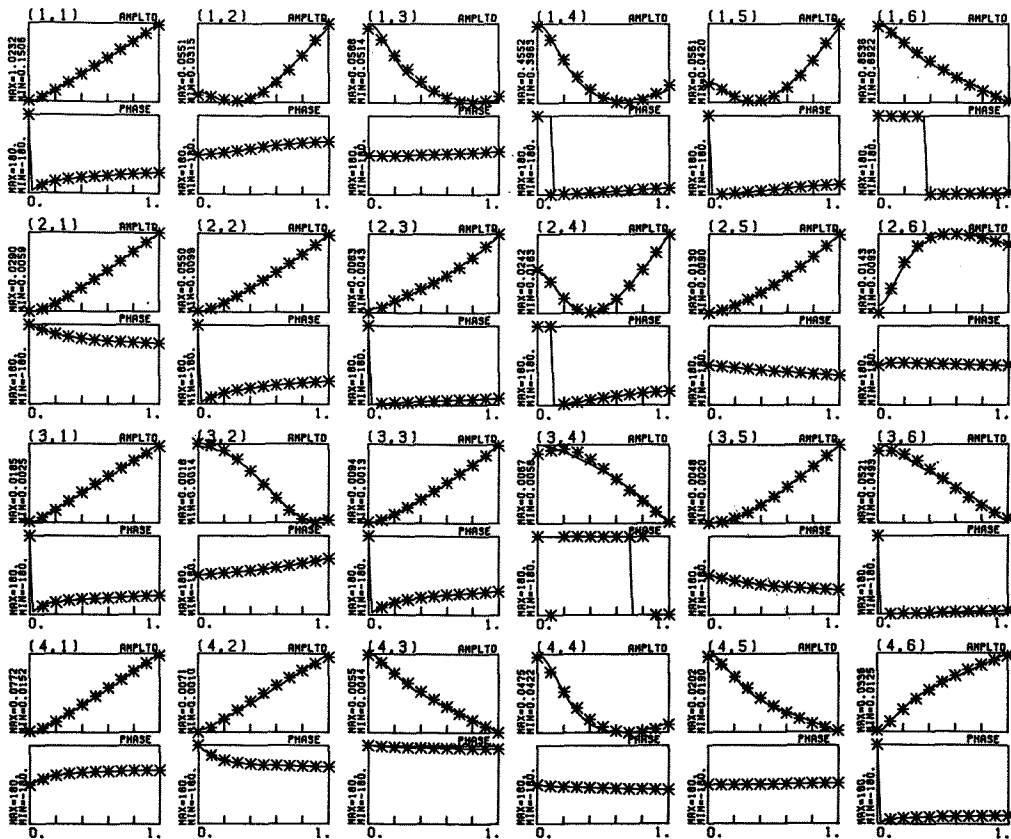
FIGURE 9.

Results of
the Aerodynamic
Modelling

Configuration 5.
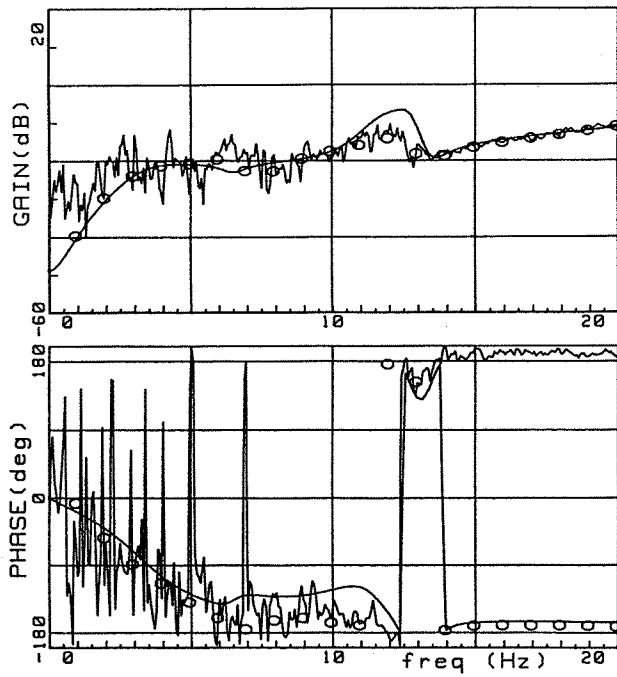
FIGURE 10. Transfer Function a_1/δ_1 (U=30m/s)

FIGURE 12. Flutter Stopper in the Tunnel
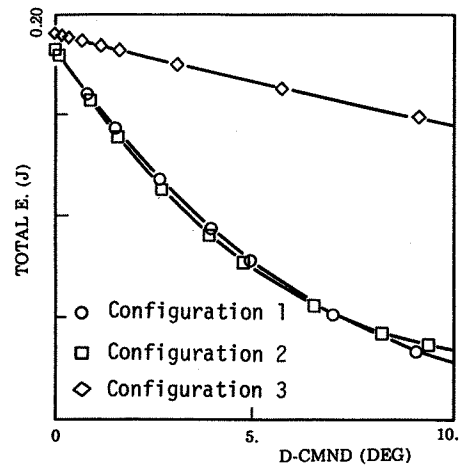
FIGURE 13. Control Effects

FIGURE 11. Schematic of the Gust Generator
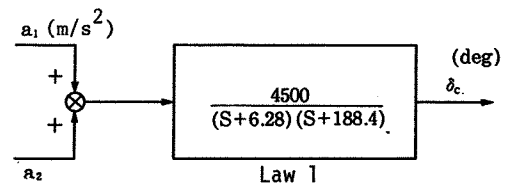
FIGURE 14. Block Diagram of Law 1
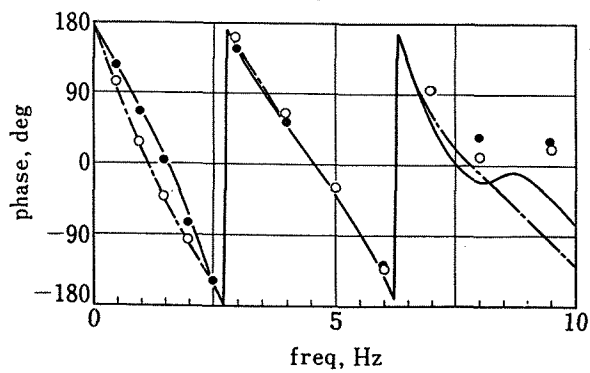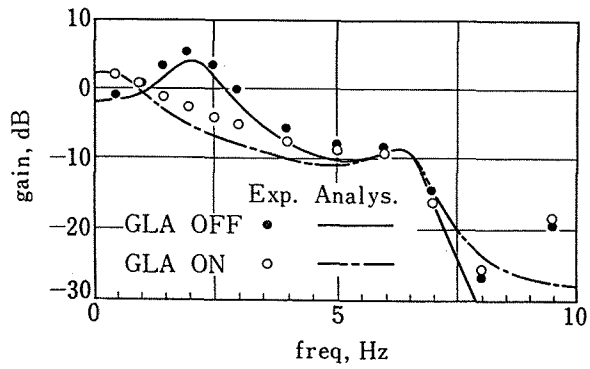
FIGURE 15. Transfer Function a_1/θ (Law 2)
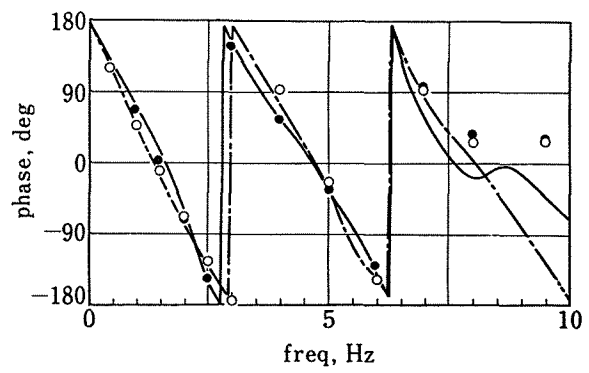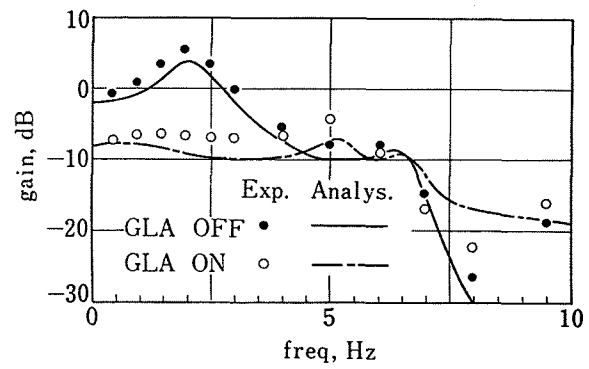
FIGURE 17. Transfer Function a_1/θ (Law 2)
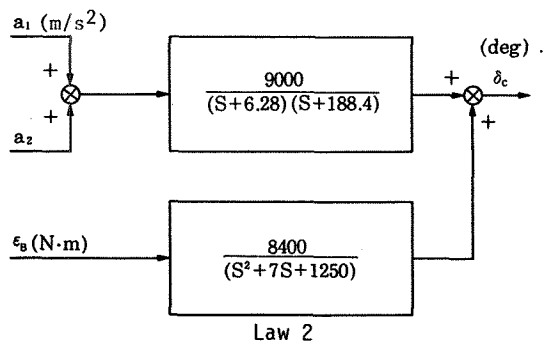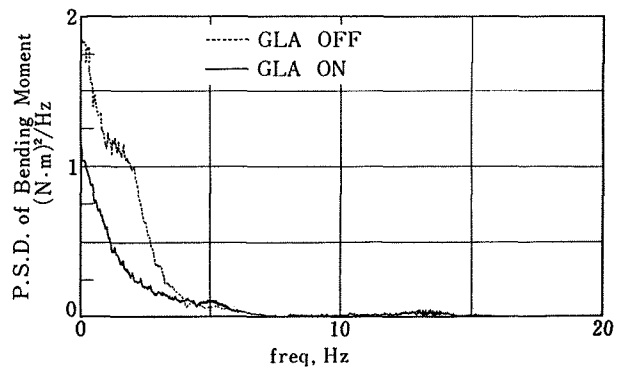

FIGURE 16. Block Diagram of Law 2

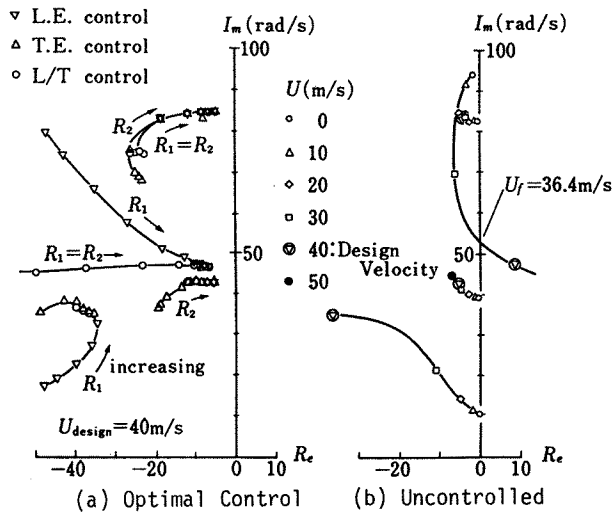

FIGURE 18. Control Effects on the Bending
Moment (Law 2)

FIGURE 19. Root Locus (Configuration 5)
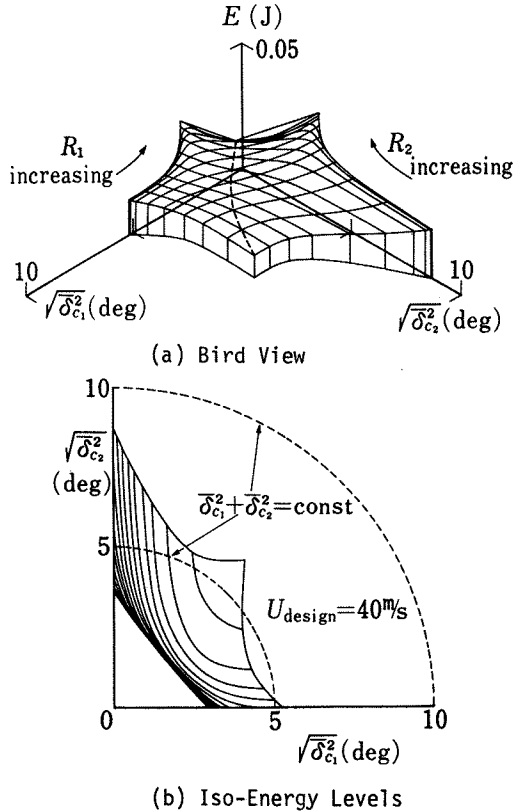

(a) Bird View

(b) Iso-Energy Levels

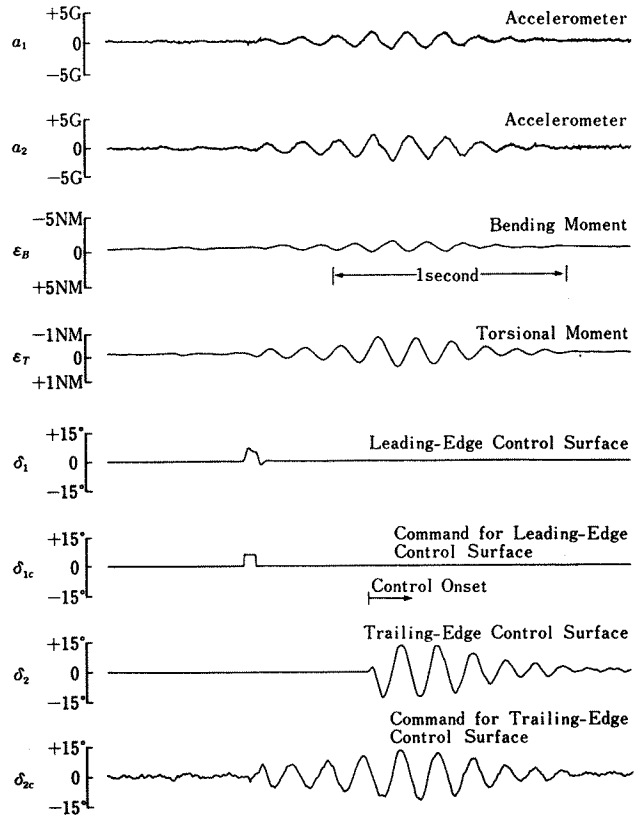FIGURE 20. Effects of Two-Degrees-of-Freedom Controls

FIGURE 21. Time Histories of Flutter Suppression (U=36.2, Law ET303)